Monthly Notices of the ROYAL ASTRONOMICAL SOCIETY

MNRAS **531,** 4432–4443 (2024) https://doi.org/10.1093/mnras/stae1446
Advance Access publication 2024 June 11

Digitally filtered resonant arguments for deep learning classification of asteroids in secular resonances

V. Carruba,[1★] S. Aljbaae,[2,3] R. C. Domingos,[4] G. Caritá,[2] A. Alves[1] and E. M. D. S. Delfino[1]

[1]*School of Engineering and Sciences, São Paulo State University (UNESP), Guaratinguetá, SP 12516-410, Brazil*
[2]*Postgraduate Division, National Space Research Institute (INPE), C.P. 515, São José dos Campos, SP 12227-310, Brazil*
[3]*Make the Way, R. Elvira Ferraz 250 - FL Office 305/306, Vila Olimpia, São Paulo, SP 04545-015, Brazil*
[4]*São Paulo State University (UNESP), São João da Boa Vista, SP 13876-750, Brazil*

Accepted 2024 June 7. Received 2024 June 7; in original form 2024 May 6

ABSTRACT

Node secular resonances, or s-type secular resonances, occur when the precession frequencies of the node of an asteroid and some planets are in commensurability. They are important for changing the proper inclination of asteroids interacting with them. Traditionally, identifying the asteroid resonant status was mostly performed by visual inspection of plots of the time series of the asteroid resonant argument to check for oscillations around an equilibrium point. Recently, deep learning methods based on convolutional neural networks (CNNs) for the automatic classification of images have become more popular for these kinds of tasks, allowing for the classification of thousands of orbits in a few minutes. In this work, we study 11 s-type resonances in the asteroid main belt and in the Hungaria region and focus on the four most diffusive ones. Two secular resonances in the Hungaria region, the $2 \cdot s - s_4 - s_6$ and the $s - 2 \cdot s_6 + s_7 - g_6 + g_8$ overlap, but this has negligible effects in terms of chaotic dynamics. Here, we obtained filtered images of the resonant arguments by filtering out all low-frequency signals with a Butterworth filter. A simple method based on amplitudes and periods of librations can perform a preliminary selection of asteroids in librating orbits. Our results show that CNN models applied to filtered images are much more effective in terms of metrics like accuracy, Precision, Recall, and F1-score than those that use images of osculating resonant arguments. Filtered resonant arguments should be preferentially used to identify asteroids interacting with secular resonances.

Key words: methods: statistical – minor planets, asteroids: general.

1 INTRODUCTION

Secular resonances occur when there is a commensurability between the precession frequencies of the longitudes of pericentre g and node s of an asteroid and the fundamental frequencies of planetary theory $g_i = \dot{\varpi}_i$ and $s_i = \dot{\Omega}_i$ (Celletti & Perozzi 2020), where i is a suffix identifying the planet, going from 2 for Venus up to 8 for Neptune, and whose values are reported in Table 1. The frequencies linked to these resonances must fulfill the equation:

$$p\dot{g} + q\dot{s} + \sum_i (p_i \dot{g}_i + q_i \dot{s}_i) = 0, \tag{1}$$

where the integers p, q, p_i, and q_i must satisfy the *D'Alembert* rules for acceptable arguments: the sum of the coefficients must be zero, and the sum of the nodal longitude frequencies must be even. 'Pericentre resonances', or g-type resonances, and 'node resonances', or s-type resonances are common names for the combinations from equation (1) that only involve the frequency of the asteroid perihelion and node, respectively.

Asteroids affected by secular resonances can be identified using various methods. First, since s-type secular resonances appear as horizontal lines in domains like (a, s), choosing asteroids in a frequency range can provide preliminary information on the more likely objects to be in resonant states. For instance, for the $\nu_6 = g - g_6$ resonance, one could search for asteroids with values of $g = g_6 \pm \Delta g$, where Δg is a cut-off level. For non-linear and higher order secular resonances, Δg is usually assumed to be equal to $0.2'' \mathrm{yr}^{-1}$ (Carruba 2009). One problem with this approach is that proper frequency values are also affected by uncertainties. As a consequence, not all asteroids in the selected range of frequencies are necessarily in resonant states. Their status needs to be confirmed by a visual inspection of the time behaviour of the resonant argument.

For an s-type resonance like the $\nu_{16} = s - s_6$, the associated resonant argument would be $\Omega - \Omega_6$. Objects in resonant states will have the resonant argument oscillate around an equilibrium point, which could be 0°, 180°, or another value. Orbits in these resonant states are called 'librating' ones, from the Latin word *libratio*, to balance. For objects outside the resonance, the resonant argument will cover all possible values, from 0° to 360° (we consider a resonant angle limited to the range from 0 to 2π). These kinds of orbits are classified as 'circulating', since the resonant arguments circulates over all possible values. Finally, because of planetary perturbations, objects near the resonance separatrix may alternate phases of circulations and libration, even when a conservative numerical integration scheme is adopted. These are the 'switching orbits'.

★ E-mail: valerio.carruba@unesp.br

Table 1. The fundamental planetary frequencies in the Solar system.

g Frequencies	Value [$''$ yr^{-1}]	s Frequencies	Value [$''$ yr^{-1}]
g_2	7.456	s_2	−7.080
g_3	17.365	s_3	−18.852
g_4	18.002	s_4	−17.633
g_5	4.257	–	–
g_6	28.243	s_6	−26.345
g_7	3.093	s_7	−2.996
g_8	0.669	s_8	−0.692

A visual analysis of plots of resonant arguments is viable when the sample of asteroids to be studied does not exceed a few hundred. It becomes rather tiresome if the number of asteroids greatly exceeds this value, and will not be viable at all when the Rubin Observatory survey discover millions of new asteroids in the Solar system (Jones, Jurić & Ivezić 2015), several thousands of which are expected to be in resonant configurations. Methods based on computer vision and the use of a perceptron artificial neural networks (ANNs) to automatically classify images of asteroids' resonant arguments were first introduced in Carruba et al. (2021c). Recently, Carruba et al. (2022) used convolutional neural networks (CNNs) and their optimizations for classifying large image data bases. This was performed for the images of osculating resonant arguments. However, such plots are affected by several low-frequency periods that may mask the long-term effect of libration around the equilibrium point and make the process of identifying librating objects more cumbersome. Low-frequency signals can be eliminated using a low-pass filter in frequency domains, like the Butterworth filter (Butterworth 1930). In this work, we aim (i) to study the most diffusive s-type secular resonances in the asteroid belt, i.e. the ones with populations of resonant objects larger than 500 asteroids, and (ii) to apply deep learning methods to images of osculating and filtered resonant arguments, and compare the effectiveness of both approaches using standard evaluating metrics in Machine Learning (ML).

2 s-TYPE SECULAR RESONANCES: LOCATION

s-type resonances occur when there is a commensurability between the precession frequency of the longitude of the node of the asteroid and other frequencies of the planets. Recently, Knežević (2022) revised what secular resonances affect the largest populations of asteroids, and made a model for their positions in proper element domains. A complete list of s-type resonances is available in Table 2. Resonances for which the value of s is higher than $s_6 = -26.345''\,\mathrm{yr}^{-1}$, the node precession frequency of Saturn, are located in the Hungaria asteroid region. The Hungaria asteroids, also known as the Hungaria group, are a population of asteroids that orbit the Sun in the inner region of the asteroid belt, primarily between the orbits of Mars and Jupiter. They are characterized by their relatively small semimajor axes, which are typically less than 1.85 au, with orbits located closer to the Sun, compared to most other asteroids in the main belt. Their name comes after the largest member of the group, 434 Hungaria, which was discovered in 1898 (Wolf 1898). Contrary to most secular resonances in the main belt, s-type resonances in the Hungaria region also involve terrestrial planets. An example is the linear resonance $s - s_4$ where there is a commensurability with the nodal precession frequency of Mars.

Three main secular resonances are observed for values of s lower than or equal to $s_6 = -26.345''/\mathrm{yr}^{-1}$: the $s - s_6$, the $s - s_6 - g_5 + g_6$, and the $s - s_6 - 2 \cdot g_5 + 2 \cdot g_6$ resonances. These resonances interact mostly with asteroids in the inner and central main belt. Table 2 displays the resonance identification used in this work, from 1 to 11, the resonant argument in terms of proper frequencies, the resonant arguments in terms of linear arguments of secular resonances (so that the $s - s_4$ is the ν_{14} resonance, and the $s - s_6 - g_5 + g_6$ is $\nu_{16} + \nu_5 - \nu_6$ resonance, with $\nu_5 = g - g_5$ and the suffixes 2, 3, 4, 5, 6, 7, and 8 identifying the planets from Venus to Neptune), the frequency value s where the resonance is found (for the $s - s_4$ resonance, $s = s_4 = -17.633''\,\mathrm{yr}^{-1}$), and the number of numbered and multi-opposition asteroids likely to be affected by the resonances. For the last two items, we use the criterion that s has to be found to within $\pm 0.2''\,\mathrm{yr}^{-1}$ from the central value since the width of the librating zone for asteroids in non-linear secular resonance tends to be less than this threshold (Carruba 2009).

The location of these secular resonances is displayed in Fig. 1 in the (a, s) plane for the main belt resonances and for the Hungarian ones. This is a good reference plane for s-type resonance, since in this domain, such resonances appear as horizontal lines, rather than having a three-dimensional structure typical of projections in the proper (a, e) or (a, $\sin(i)$) domains (Carruba & Michtchenko 2007).

Not all the resonances listed in Table 2 may have a population of asteroids in librating states large enough to warrant a viable deep-learning CNN model, which is of the order of at least a few hundred asteroids. To select the resonances most appropriate for our study, we numerically integrate the first 200 asteroids that fulfill the frequency cut-off criterion under the influence of all planets for 10 Myr, using the numerical set-up described in Carruba et al. (2021c). At this stage, we neglected the influence of massive bodies in the main belt because the gravitational influence of these objects is not large enough to significantly modify the position of secular resonances in proper elements domains, and the possible scattering caused by close encounters with such bodies could needlessly complicate the problem of identifying images of resonant arguments (Carruba et al. 2024). For each resonance with a preliminary population larger than 200 asteroids listed in Table 2, we plotted the resonant arguments of the 200 simulated objects and verified the fraction of librators for each set of the simulated objects. We then computed the mean fraction and the uncertainty assumed equal to the standard deviation, for the whole set of 200 objects and used this information to extrapolate the possible range of values for the librating population among numbered and multi-opposition asteroids. The last two columns in Table 2 report these data.

Only three resonances have an estimated population of librators larger than 500, and are therefore suitable for modellization with computer vision. These are the $s - s_6 - 2 \cdot g_5 + 2 \cdot g_6$, the $2 \cdot s - s_4 - s_6$, and the $s - s_6 - g_5 + g_6$ resonances, in descending order of estimated populations. We will concentrate our attention on these resonances hereafter, whose identifications are summarized in Table 3. Interestingly enough, three resonances in the Hungaria region have small populations of librators and could be interesting subjects for future dynamic studies. These are the $s - 2 \cdot s_6 + s_7 - g_6 + g_8$, $s - 2 \cdot s_8 + s_7 - g_5 + g_6$, and the $s - s_6 - g_5 + g_8$ resonances. s-type secular resonances in the Hungaria region overlap among themselves, with cases of objects alternating phases of libration in two or three different secular resonances. Because of its possible dynamical importance for its interaction with the $2 \cdot s - s_4 - s_6$ resonance, we will also study in this work the $s - 2 \cdot s_6 + s_7 - g_6 + g_8$ resonance (see Table 3).

Fig. 2 displays results for numbered objects. We only display asteroids for which the errors in proper s are less than 0.2 arcsec

Table 2. The most diffusive s-type secular resonances in the main belt, according to Knežević (2022). We report the resonant argument in terms of frequencies, in terms of combinations of linear secular resonances, the central value of the asteroidal s frequency associated with each resonance, the number of asteroids, numbered and multi-opposition, likely to be affected by the resonances, the fractions of librators among the first 200 numbered candidates, and the extrapolated number range of possible librators.

Res. id.	Res. argument frequencies	Res. argument linear resonances	Frequency value [$''$ yr^{-1}]	Numbered ast.	Multi-opp. ast	Fract. of libr.	Extr. Number of libr.
1	$s - s_4$	ν_{14}	−17.633	1	6	–	–
2	$2 \cdot s - s_4 - s_6$	$\nu_{16} + \nu_{14}$	−21.989	1833	2135	28.5 ± 14.6	1131 ± 580
3	$s - 2 \cdot s_4 + s_7 - g_6 + g_4$	$2 \cdot \nu_{14} - \nu_{17} + \nu_6 - \nu_4$	−22.029	1853	2129	0.0 ± 0.0	0.0 ± 0.0
4	$s - 2 \cdot s_6 + s_7 - g_6 + g_8$	$2 \cdot \nu_{16} - \nu_{17} + \nu_6 - \nu_8$	−22.120	1925	2157	$4.0^{+6.0}_{-4.0}$	163^{+245}_{-163}
5	$s - s_3 - g_5 - g_6 + 2 \cdot g_4$	$\nu_3 + \nu_5 + \nu_6 - 2 \cdot \nu_4$	−22.357	1730	1857	0.0 ± 0.0	0.0 ± 0.0
6	$s - 2 \cdot s_8 + s_7 - g_5 + g_6$	$2 \cdot \nu_{18} - \nu_{17} + \nu_5 - \nu_6$	−22.375	1741	1950	$4.5^{+5.0}_{-4.5}$	166^{+188}_{-166}
7	$s - s_3 - g_8 + g_5$	$\nu_{13} + \nu_8 - \nu_5$	−22.439	1707	1841	0.0 ± 0.0	0.0 ± 0.0
8	$s - s_6 - g_5 + g_8$	$\nu_{16} + \nu_5 - \nu_8$	−22.758	1476	1530	$7.0^{+8.0}_{-7.0}$	225^{+255}_{-225}
9	$s - s_6$	ν_{16}	−26.345	20	24	–	–
10	$s - s_6 - g_5 + g_6$	$\nu_{16} + \nu_5 - \nu_6$	−50.332	4899	3498	46.5 ± 15.7	3904 ± 1310
11	$s - s_6 - 2 \cdot g_5 + 2 \cdot g_6$	$\nu_{16} + 2 \cdot \nu_5 - 2 \cdot \nu_6$	−74.319	2588	2170	11.5 ± 9.9	547 ± 471

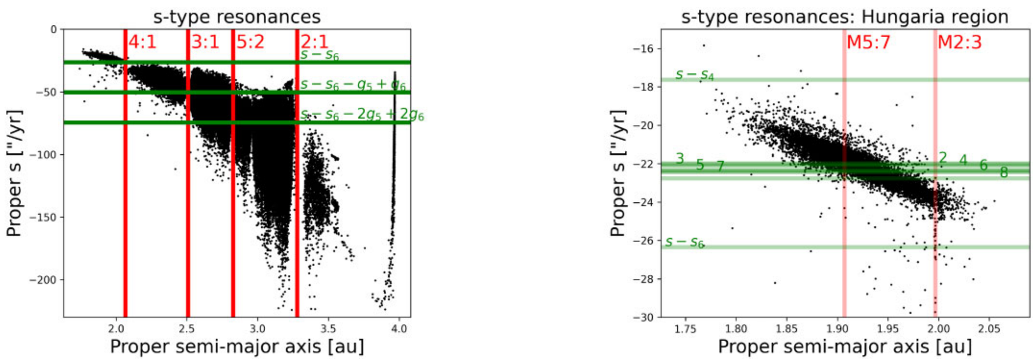

Figure 1. Left panel: a projection in the (a, s) plane of the location of the three main s-type resonances in the main belt, as reported in Table 2. Right panel: the same projection for the Hungaria asteroids' region. The numbers in the figure identify the resonances, according to the nomenclature in Table 2. Vertical red lines display the location of important local mean-motion resonances.

Table 3. The most populated s-type secular resonances in the main belt, according to this study. We report the resonant argument in terms of frequencies and in terms of combinations of linear secular resonances.

Res. id.	Res. argument frequencies	Res. argument linear resonances
S2	$2 \cdot s - s_4 - s_6$	$\nu_{16} + \nu_{14}$
S4	$s - 2 \cdot s_6 + s_7 - g_6 + g_8$	$2 \cdot \nu_{16} - \nu_{17} + \nu_6 - \nu_8$
S10	$s - s_6 - g_5 + g_6$	$\nu_{16} + \nu_5 - \nu_6$
S11	$s - s_6 - 2 \cdot g_5 + 2 \cdot g_6$	$\nu_{16} + 2 \cdot \nu_5 - 2 \cdot \nu_6$

yr^{-1}, which is the limit used to select asteroids affected by s-type resonances. Results for multi-opposition asteroids are similar and will not be shown for the sake of brevity. The S2 resonance has a dynamic effect on the asteroids that interact with it, producing a higher number density of objects near its centre, which also translates into a higher number density of librating asteroids. As expected, the higher order S4 resonance has a less marked dynamic effect, with a low number density of objects near its centre and a more sparse population of librating asteroids. Because of the very limited distances in frequencies between the two resonances, of less than 0.09 arcsec yr^{-1}, resonance overlapping is possible for these two resonances.

For instance, Fig. 3 shows the resonant arguments for the S2 (left panels) and S4 (right panels) resonances, for an asteroid in librating states of the S2 resonance (55844 Bicak, top panels) and for one inside the S4 resonance (262918 (2007 CA62), bottom panels). It is possible for an asteroid to be in a resonant state of the S2 or S4 resonances, and to be in either a librating or a switching orbit of the other resonance at the same time. For the S2 resonance, we found among numbered asteroids 152 objects in pure librating states, 364 also in switching orbits of the S4, and 133 that were librating in both resonances. For the S4 resonance, there were 84 numbered asteroids in pure librating states, 37 that were also in S2 switching orbits, and, again, the 133 librating in both states of the S2 and S4.

The superposition of secular resonances observed for these asteroids does not appear to produce any observable effect in terms of chaotic dynamics. We obtained Lyapunov times, as provided by the Asteroid Families Portal *AFP* ('http://asteroids.matf.bg.ac.rs/fam/index.php'; Radović et al. 2017; Novaković et al. 2022, accessed on November 2023), and ACFI (Carruba et al. 2021a) chaos indicator obtained by means of numerical simulations for asteroids in pure S2 and S4 states and for the 133 objects that are in both resonances. Lyapunov times, also known as Lyapunov exponents or characteristic Lyapunov time-scales, are measures used in the field of dynamic systems to

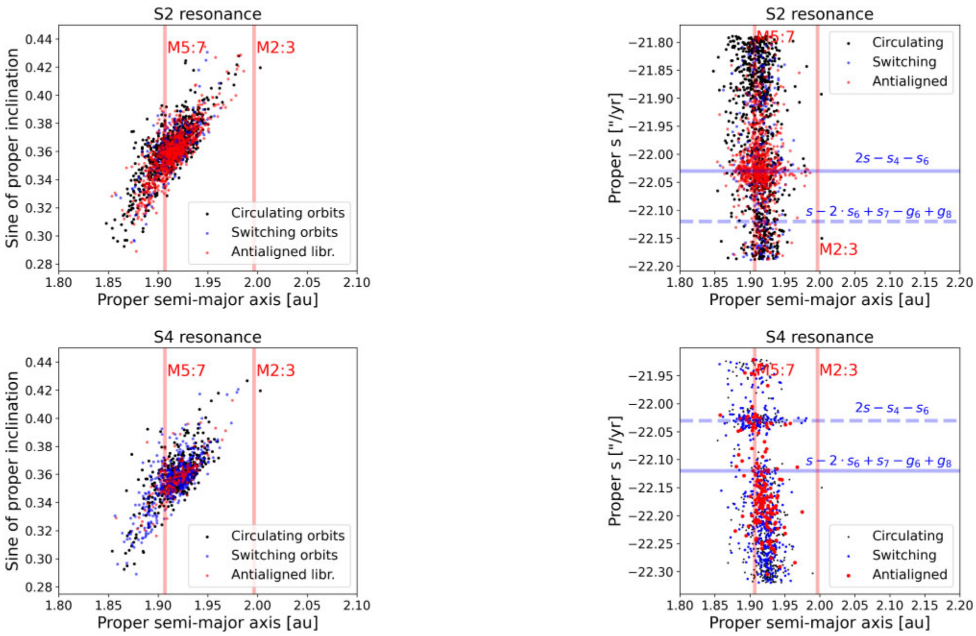

Figure 2. Proper (a, $\sin(i)$) and (a, g) projections of numbered asteroids with errors in proper $s < 0.2$ arcsec yr^{-1} for bodies in the S2 (top panels) and S4 (bottom panels) resonances, in the Hungaria region. The vertical lines display the location of important local mean-motion resonances. Horizontal lines in the right panels show the location of the two secular resonances of interest, S2 and S4.

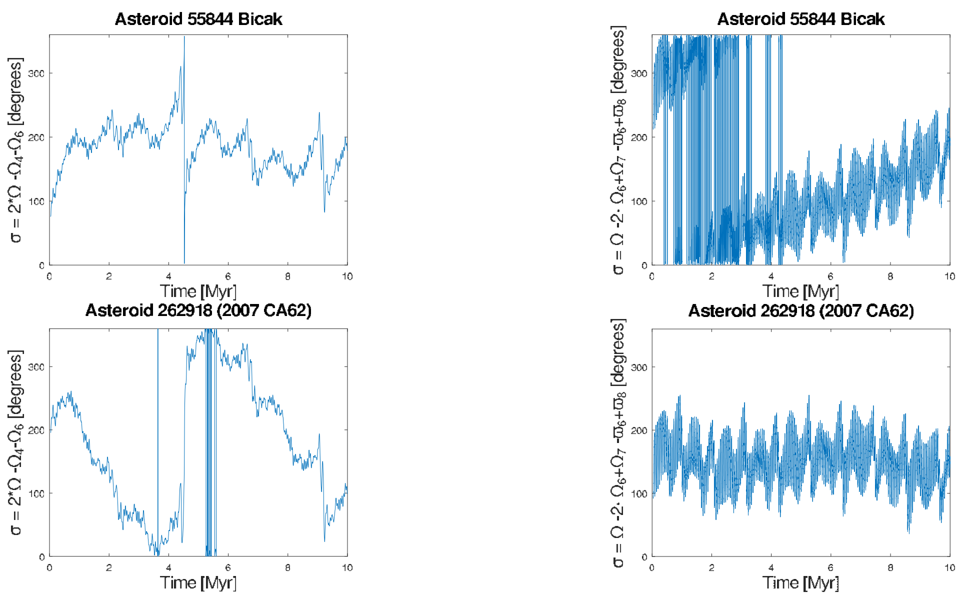

Figure 3. Resonant arguments for the $2 \cdot s - s_4 - s_6$ (left panel) and $s - 2 \cdot s_6 + s_7 - g_6 + g_8$ (right panel) for the asteroids 55844 Bicak (top panels) and 262918 (2007 CA62) (bottom panels).

quantify the rate of exponential divergence of nearby trajectories in a chaotic system. They provide a way to assess the predictability and sensitivity to initial conditions in chaotic systems. The ACFI (autocorrelation function indicator) is a chaos indicator that identifies chaotic behaviour in dynamic systems. It is based on analysing the autocorrelation function of a time series generated by the system. Our results for the Lyapunov times are shown in Fig. 4. We applied the Kolgomorov–Smirnoff (KS, Kolmogorov 1933) test to the distributions of Lyapunov times for the asteroids in both resonances and for objects in pure S2 and S4 resonant states to verify if they could come from different statistical distributions. Our results show that the two groups are statistically indistinguishable, with p-values quite above the 0.05 level needed to confirm that the two populations could come from different distributions. ACFI values are also consistent with this analysis; results will not be shown for the sake of brevity. If there is any effect produced by secular resonance overlapping for the S2 and S4 resonances, it is not observable in our data.

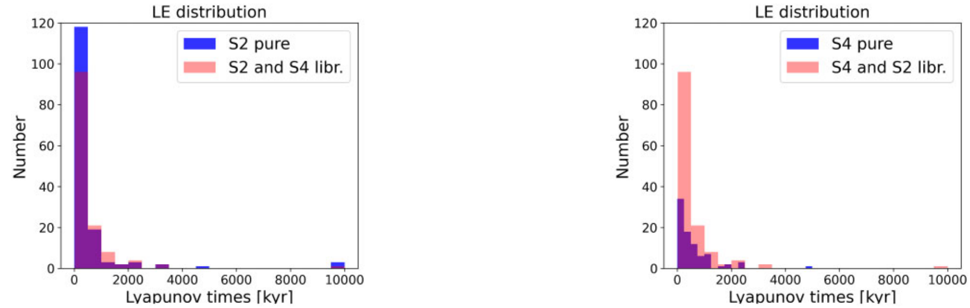

Figure 4. Distribution of Lyapunov times for objects in pure S2 and in both S2 and S4 librating states (left panel). The right panel shows the same, but for asteroids in the S4 resonance.

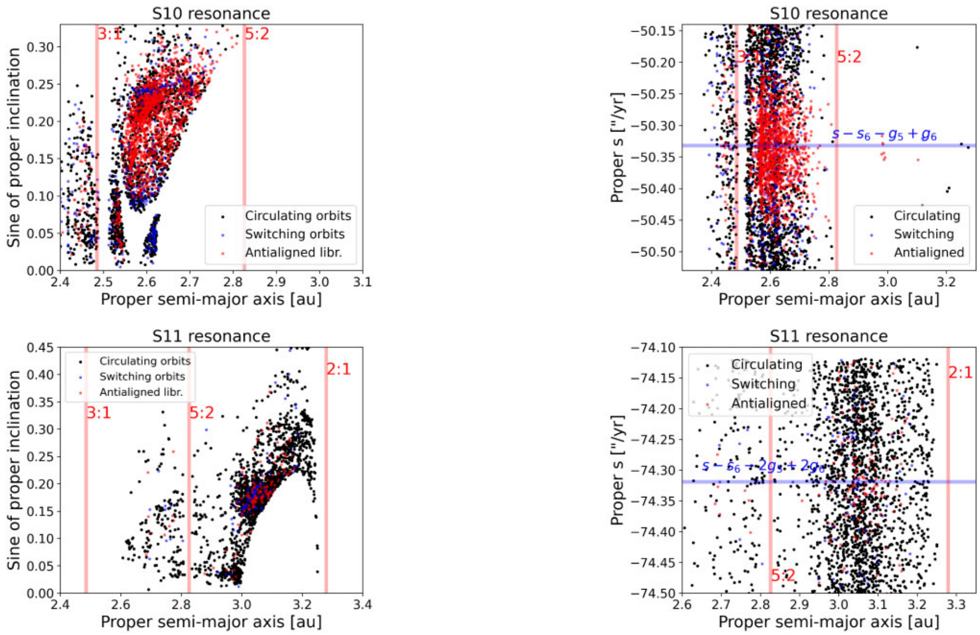

Figure 5. The same as Fig. 2, but for the S10 and S11 resonances.

Concerning main belt resonances, in Fig. 5, we report results for the S10 and S11 resonances. The S10 resonance is a dynamically highly diffusive resonance with a large population of libration concentrated towards the resonance central value in proper s. Most of the librating population for this resonance is found in the central main belt. The S11 resonance is a less diffusive resonance, with fewer librating asteroids. Most of the S11 librators are found in the outer main belt.

3 IMAGES OF RESONANT ARGUMENTS

Since we are interested in studying the $s - s_6 - g_5 + g_6$ secular resonance, the associated resonant argument is $\Omega - \Omega_6 - \varpi_5 + \varpi_6$, where Ω is the longitude of the node, ϖ is the longitude of pericentre, and the suffixes 5 and 6 stand for Jupiter and Saturn, respectively. From the output of the numerical simulations we can produce time series of the resonant argument. These will be the product of superpositions of short- and long-period terms. Since we are interested in secular effects, we can apply a low-pass filter in frequency domains, like the Butterworth filter (Butterworth 1930), to allow low-frequency signals to pass through while attenuating high-frequency signals. This filter will allow signals with frequencies below a specified cut-off frequency value to pass through with minimal attenuation. The steepness of the roll-off in the stopband, which is the range of frequencies above the cut-off frequency that are attenuated by the filter, is determined by the order of the filter. The higher the order of the filter, the steeper the roll-off in the stopband.

A Butterworth filter is designed to have a maximally flat frequency response in the passband, which means that it has no ripple in the passband and the transition from the passband to the stopband is as smooth as possible. This gives the filter a very flat response in the passband. At the same time, the filter has a steep roll-off in the stopband, which means that it can effectively attenuate high-frequency noise or unwanted signals that may be present in the input signal.

Since our data are sampled in time every 600 yr, the filter has a sampling frequency of $f_s = 1\ /\ (600\ \mathrm{yr}) = 1.67 \times 10^{-4}$ Hz. The Nyquist frequency is the highest frequency that can be accurately represented in a digital signal processing system that samples a continuous-time signal at a fixed rate. It is defined as half the sampling rate or half the frequency at which the signal is being sampled, which in our case is 8.3×10^{-5} Hz. An appropriate

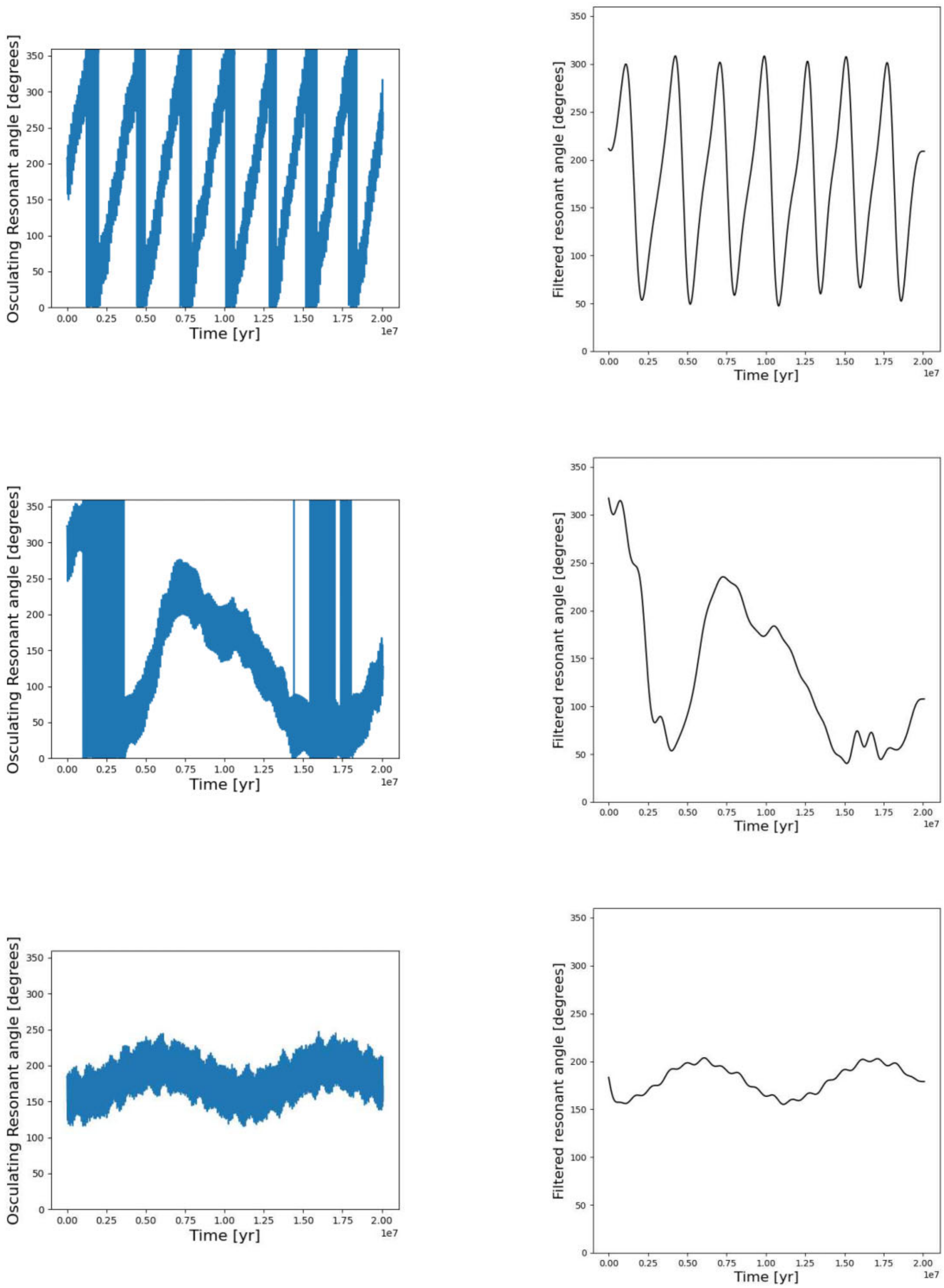

Figure 6. The left panels display images of the osculating resonant argument of the $s - s_6 + g_6 - g_5$ secular resonance, while the right panels do the same for the filtered arguments. From top to bottom, we show images of resonant arguments for circulating, switching, and librating orbits.

cut-off frequency would have to be less than one-tenth of the Nyquist frequency. In our case, we use a cut-off value of 1×10^{-6} Hz.

Fig. 6 shows examples of the time behaviour of resonant angles for the osculating case (left panels) and for the cases where we applied our low-pass filter (right panels). We show examples of asteroids in orbits for which the resonant argument circulates from 0° to 360°, alternates phases of circulations and oscillations around an equilibrium point ('switching orbits'), and of orbits for which the resonant argument oscillates around an equilibrium point at 180° ('librating orbits'). Librating orbits tend to have a smaller oscillation amplitude and longer periods of the resonant argument than circulating ones. Switching orbits behaviour in terms of amplitudes and periods tend to be overlapping the circulating and librating cases.

Based on these considerations, can a simple criteria for selecting librating orbits be defined in terms of amplitudes and periods to be

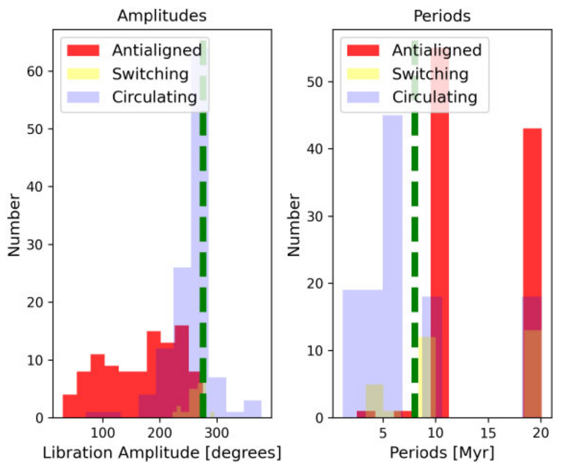

Figure 7. Histograms of libration amplitudes and periods for asteroids in librating, circulating, and switching states of the S10 resonance. The vertical dashed line represents the cut-off value of the maximum amplitude (left panel) and minimum period (right panel) for librating orbits.

used for selecting such cases? We selected a sample of the first 250 numbered asteroids affected by the S10 resonance, and applied our code to filter the resonant arguments and obtain their amplitudes and periods. Fig. 7 shows our results. To select librating asteroids, we selected objects that (i) have amplitudes smaller than the maximum observed for librating objects and (ii) have periods larger than 8 Myr. Both these conditions appear to characterize most of the identified librating population. This procedure was repeated for the S2, S4, and S11 resonances.

To quantify the performance of this method, we applied metrics commonly used in machine learning. A true positive (*TP*) in binary classification happens when the model predicts a positive class and the real value is, in fact, positive. When the model predicts a positive class but the actual value is negative, this is known as a false positive (*FP*). When the model predicts a negative class but the actual value is positive, this is known as a false negative (*FN*). Lastly, when both the expected and actual values are negative, true negatives (*TN*) happen. For our case, a positive result would be a librating object, and a negative a circulating or switching asteroid. This is not a generally accepted practice, and other authors assign switching orbits to the librating class (Murray & Dermott 1999). Since previous experience showed that most switching orbits tend to become circular ones when the Yarkovsky force is considered, we prefer here to follow the practice introduced in previous works from our group (Carruba et al. 2024).

The classifier's overall performance is generally measured by *Accuracy*, which shows the percentage of accurate predictions. If the data set is unbalanced, meaning one class predominates over the others. This could be deceptive if the data set is unbalanced, meaning one class predominates over the others. *Accuracy* is defined as

$$Accuracy = \frac{TP + TN}{TP + TN + FP + FN}. \tag{2}$$

This can also be computed as the fraction of correct predictions divided by the total number of predictions. The percentage of accurately predicted positive cases among all positively predicted instances is measured by a statistic called *Precision*. It highlights the real positives and shows how well the classifier can weed out false positives. The formula for *Precision* is as follows:

$$Precision = \frac{(TP)}{(TP + FP)}. \tag{3}$$

The percentage of accurately predicted positive cases among all actual positive instances is measured by *Recall*, which is sometimes referred to as sensitivity or true positive rate. Its main goal is to find all positive examples and stay away from false negatives. *Recall* is given by

$$Recall = \frac{(TP)}{(TP + FN)}. \tag{4}$$

Finally, the $F1$ score is the harmonic mean of precision and recall. It provides a balanced measure that combines both precision and recall into a single metric. The F1 score is calculated using the following formula:

$$F1 = 2 * \frac{(Precision * Recall)}{(Precision + Recall)}. \tag{5}$$

Table 4. Classification in terms of accuracy, precision, recall, and F1-score for the population of the first 250 numbered asteroids inside the four studied *s*-type resonances, using the criterion based on maximum oscillation amplitude and resonant period (first four entries) and from the results of *ML* model optimized using genetic algorithms in the domain of proper *s*, Amplitude, and Period (last four entries).

Res. id.	Accuracy	Precision	Recall	F1
S2	82.4	60.4	88.7	71.9
S4	53.6	15.7	100.0	27.1
S10	82.8	70.5	98.0	82.0
S11	60.8	17.8	95.5	30.0
S2	80.0	100.0	37.5	54.5
S4	98.0	0.0	–	–
S10	92.0	82.4	93.3	87.5
S11	88.0	60.0	42.9	50.0

The F1 score ranges from 0 to 1, where a value of 1 indicates the best performance, balancing precision, and recall. The first four entries of Table 4 display our results for the four resonances, in terms of the four metrics. Values of *Precisions* tend to be lower than *Recall* and *Accuracy*. The method tends to retrieve a large fraction of the librating asteroids, but it also identifies as librators circulating and switching orbits with low amplitudes and long periods. This approach tends to perform better for 'stronger' secular resonances, i.e. resonances for which there is a large fraction of librators, like the S2, and S10. *Accuracy* and *Precision* are particularly low for the S4 and S11 resonances, which have fractions of librators below 15 per cent.

Overall, this simple approach can be thought of as a base model.[1] Any results of deep learning approaches will have to be better than what this simpler criterion produces. Based on the analysis of these results, which show the importance of computing periods and maximum oscillation amplitude, we decided also to devise an *ML* model that uses these quantities and the proper s value. Since librating asteroids tend to cluster close to the central frequency value of each resonance, as listed in Table 2, fourth column, we

[1] Recent work showed that the accuracy of similar approaches can be improved by including additional parameters like the number of border crossings, the libration time, etc. (Smirnov 2023). This optimization, however, requires an ad hoc, more in depth study for each resonance, which, in our opinion, exceeds the purposes of this work. A more in-depth analysis remains an interesting topic for future research.

Table 5. We report the number of asteroids in class 0, class 1, and the imbalance ratios between class 0 and class 1 for the asteroid data bases studied in this work.

Data base name	Class 0 # of ast.	Class 1 # of ast.	Imbalance ratio
S2	1105	745	2.5
S4	1539	311	4.9
S10	3236	1653	2.0
S11	2351	249	9.4

believe that an *ML* approach based on these three variable could also produce a good outcome. Using genetic algorithms (Chen, Wang & Lee 2004), we pick the top-performing *ML* techniques and the set of its free parameters, or hyperparameters, that perform best for our data set, following the steps outlined in Carruba, Aljbaae & Domingos (2021b). Three iterations of the genetic algorithm process are applied to a selection of asteroids, with a validation set of 20 per cent of the training data. The use of a validation set is advised to prevent the problem of overfitting, which arises when the model is very sensitive to the minute details of the training set yet may perform poorly when dealing with different sets of data.

The four best-performing *ML* models for the S2, S4, S10, and S11 data bases were the Gaussian Naive Bayesian, Decision Tree, GradientBoostingClassifier (GBoost), and MLPClassifier, respectively. For the Gaussian Naive Bayesian model, we used a pipeline with the *SelectPercentile* routine using the *score_func* = *f_classif*, and a percentile of 76, and the default version of the Gaussian Naive Bayesian model. For the Decision Tree we used the *gini* criterion, a max_depth of 3, a min_samples_leaf of 19, and a min_samples_split of 17. For the GBoost method, we used learning_rate=0.5, max_depth=1, max_features=0.6, min_samples_leaf=14, min_samples_split=2, n_estimators=100, subsample=0.9. Finally, for the MLPClassifier we used a pipeline with a *RobustScaler()* and *StandardScaler* routines, and values of alpha=0.0001 and learning_rate_init=0.001 for the MLPClassifier hyperparameters. Interested readers are referred to the reference page of the SCIKIT-learn PYTHON library (Pedregosa et al. 2011) for more details on the theory behind these classifiers and their hyperparameters.

Our results are displayed in the last four entries of Table 4. The *ML* model outperforms the simpler approach based on periods and amplitudes for the case of the strong S10 resonance in all metrics but Recall tends to perform more poorly for the other, weaker resonances. Overall, the simpler approach could be a better choice for a preliminary analysis of these kinds of data sets.

In the next section, we will investigate the use of CNN models for the problem of identifying resonant asteroids in *s*-type secular resonances.

4 CONVOLUTIONAL NEURAL NETWORK MODELS

Before applying machine learning methods to the data bases of images of resonant arguments obtained in this work, we checked if any of these data sets can be affected by a severe imbalance between the librating class of orbits, defined as 1, and the rest, class 0. We define an imbalance ratio as the number of objects in class 0 divided by the number of objects in class 1. Standard machine learning approaches may not be working properly for data sets with a severe imbalance, which is a ratio higher than 100 (Brownlee 2020). Our results for numbered asteroids are shown in Table 5. None of the data sets is affected by a severe imbalance, and, also based on experience with other data bases for asteroids interacting with resonant configurations (Carruba et al. 2023), none of the methods for dealing with imbalanced data sets are likely to significantly improve the outcome of *ML* models.

We therefore turned our attention to methods for image classification, to classify the data sets for the S2, S4, S10, and S11 resonances. Following the approach of Carruba et al. (2022), we use three models of CNNs: the Visual Geometry Group (VGG) (Simonyan & Zisserman 2014), the Inception (Szegedy et al. 2015), and ResNet (He et al. 2016) models to study two data sets of images of resonant arguments, the osculating, and the filtered ones. We refer interested readers to Carruba et al. (2022) for details on the model's architectures. To avoid possible misclassification issues caused by the filtering, which occasionally can transform circulating orbits into librating ones (see for instance the top panels of Fig. 6), the images' labels are those obtained by the analysis of the osculating images.

For all data bases, we divided our data sets into a training, a validation, and a test set, following the same approach of Carruba et al. (2024) for the sizes of the data bases. Namely, the training set will be composed of numbered asteroids up to identification 500 000, the validation set of asteroids with identification between 500 000 and 600 000, and the test set will have asteroids with identifications larger than 600 000. The presence of a validation set is needed to ensure that the model is not overfitting. If values of accuracy and loss of the training set are higher and lower than those of the validation set, the model is learning all the fine details of the training set data, but may not be able to efficiently export its performance to other data sets. Regularization methods like data augmentation and dropout, which involve to artificially increase the size of a training data set by applying various transformations such as rotation, translation, scaling, flipping, and cropping to the input images or by randomly setting a fraction of the output features of a layer to zero during the training phase, can then be applied to avoid overfitting issues. Interested reader can find more details on the implementation of Data Augmentation (DA) and Dropout (DO) in Carruba et al. (2022).

Our results for the S10 resonance are shown in Table 6. Similar tables were obtained for the S2, S4, and S11 resonances and are available in Appendix A. Generally, CNN performs much better in domains of filtered arguments than in spaces of osculating ones, and better for less imbalanced data bases like those of the S10 and S2 resonances.

For each resonant data base, we selected the model that (i) most outperformed the simple period–amplitude criterion discussed in section (3), and (ii) was less affected by the problem of overfitting. For the S10 resonance, for instance, four models applied to filtered images had a better performance in terms of accuracy and F1 score than the period–amplitude criterion, which scored 82.6 in terms of F1: VGG+DA (F1 = 85.7), ResNet (F1=90.0), VGG (F1=90.5), and Inception (F1=97.6).

Fig. 8 displays the loss function and accuracy epoch-wise of the two top-performing models in the S10 resonance data base. Both models are affected by overfitting, but the Inception model has a higher F1 score. For this resonance, we therefore selected the Inception model. We then performed a similar analysis for the other resonance data bases. All models for the S2 with filtered arguments had the same performance, but the Inception + DA + DO model was the less affected by overfitting, and was the selected model for this resonance. For the S4 resonance, the best-performing model both in terms of scores and being less prone to overfitting was the VGG model. Finally, for the S11 resonance, the VGG model, although slightly affected by overfitting issues was again the best-performing one.

Table 6. Classification in terms of accuracy, precision, recall, and F1-score for the results obtained by CNN models for samples of unfiltered (U) and filtered (F) images of the S10 resonant arguments. The last three columns report the execution time, memory, and maximum memory allocation observed using an 11th Gen Intel(R) Core(TM) i7-11700F @ 2.50GHz CPU. Memory allocations are measured in gigabytes (GB).

Model	Accuracy	Precision	Recall	F1	Time [m:s]	Memory alloc. [GB]	Max. Memory alloc. [GB]
VGG (U)	72.0	61.5	80.0	69.5	10:50	3.98	10.29
VGG+DA (U)	62.0	52.2	60.0	55.8	10:53	3.98	10.29
VGG+DA+DO (U)	62.0	51.9	70.0	59.6	11:39	3.99	10.29
Inception (U)	74.0	63.0	85.0	72.3	11:19	3.98	10.29
Inception+DA (U)	62.0	51.6	80.0	62.7	11:21	3.99	10.29
Inception+DA+DO (U)	62.0	51.6	80.0	62.7	12:05	4.34	10.29
ResNet (U)	62.0	51.6	80.0	62.7	13:23	3.98	10.53
ResNet+DA (U)	62.0	51.6	80.0	62.7	13:13	3.99	10.54
ResNet+DA+DO (U)	62.0	51.6	80.0	62.7	14:16	4.34	10.86
VGG (F)	92.0	86.4	95.0	90.5	11:01	3.98	10.29
VGG+DA (F)	90.0	100.0	75.0	85.7	11:08	3.98	10.29
VGG+DA+DO (F)	76.0	90.0	45.0	60.0	11:41	3.99	10.29
Inception (F)	98.0	95.2	100.0	97.6	10:08	4.30	10.29
Inception+DA (F)	76.0	83.3	50.0	62.5	11:37	3.99	10.29
Inception+DA+DO (F)	82.0	100.0	55.0	71.0	11:48	3.99	10.29
ResNet (F)	90.0	90.0	90.0	90.0	12:59	3.98	10.53
ResNet+DA (F)	72.0	80.0	40.0	53.3	12:45	3.98	10.54
ResNet+DA+DO (F)	86.0	84.2	80.0	82.1	13:36	4.30	10.86

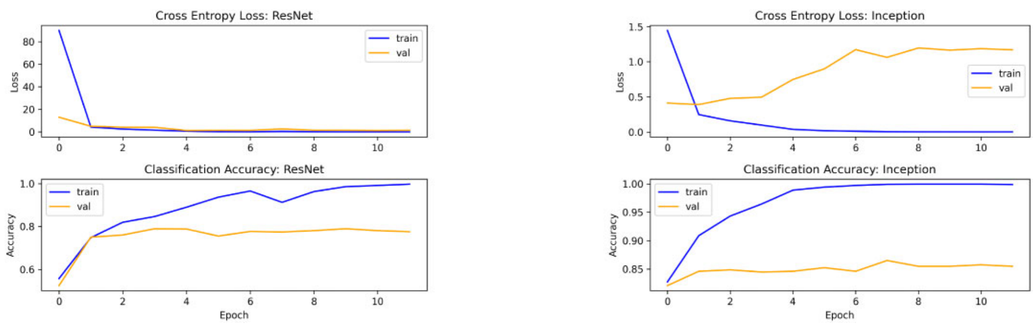

Figure 8. The behaviour in terms of the epoch of the loss function and accuracy for the two best-performing models for the S10 resonance data base.

Table 7. The best performing CNN models for each resonance, classified in terms of F1 score and overfitting.

Resonance ID	Best-performing model	F1 score	Overfitting
S2	Inception + DA + DO	80.0	No
S4	VGG	54.5	No
S10	Inception	97.6	Yes
S11	VGG	83.3	Yes

Table 7 summarizes our results. The best-performing models tend to be either VGG or Inception ones, all applied to filtered resonant arguments.

5 CONCLUSIONS

In this work, we investigated the asteroidal population that interacts with secular resonances of s-type. For each resonance, we selected asteroids whose values of s is within $\pm 0.2'' \mathrm{yr}^{-1}$ from the central value. We then visually inspected the time behaviour of each resonant argument. Of the 11 s-type resonances listed by Knežević (2022), only four resonances, the $2 \cdot s - s_4 - s_6$ (identified in this work as S2 for brevity), the $s - 2 \cdot s_6 + s_7 - g_6 + g_8$ (S4), the $s - s_6 - g_5 + g_6$ (S10), and the $s - s_6 - 2 \cdot g_5 + 2 \cdot g_6$ (S11) have a population of librators larger than 500, and are therefore suitable for modellization with computer vision.

The S2 and S4 secular resonances in the Hungaria region overlap with each other, and we found a population of objects in librating states of both resonances. This new kind of resonance overlapping is, however, not conducting to chaos. We computed Lyapunov exponents and ACFI chaos indicators for asteroids not in resonances and for those in librating states of both the S2 and S4 resonances. No significant differences between the two populations were observed, suggesting that this resonance overlapping does not introduce any chaos in the dynamics of the affected asteroids.

We then turned our attention to deep learning models for identification of asteroids interacting with secular resonances. We applied a Butterworth filter (Butterworth 1930) to eliminate short-period terms, and devised an approach to identify librating asteroids assuming that (i) their libration amplitude was smaller than the maximum amplitude observed for librating objects, and (ii) that they had periods larger than 8 Myr. The efficiency of this simple approach, or base model, was then measured using standard metrics of *ML*, like *Accuracy*, *Precision*, *Recall*, and *F*1 score. This approach performed best for more populated resonances, like the S2 and S10.

ML methods optimized through the use of genetic algorithms were then used. For the case of the strong S10 resonance, the *ML* model fared better than the more straightforward method based on periods and amplitudes in every metric except *Recall*; however, it tended to perform worse for the other, weaker resonances. For a preliminary examination of these kinds of data sets, the more straightforward method might be preferable.

Finally, CNN methods for computer vision, like the VGG (Simonyan & Zisserman 2014), the Inception (Szegedy et al. 2015), and ResNet He et al. (2016) models were applied to the newly developed data bases for both osculating and filtered elements. To avoid overfitting issues, a validation data set was set apart, and regularization methods like data augmentation and dropout, were also applied consistently. In all cases, the performance of CNN models was superior when applied to images of filtered resonant arguments. Based on these results, asteroids interacting with secular resonances should be identified using a computer vision approaches primarily through the use of filtered resonant arguments.

ACKNOWLEDGEMENTS

We are grateful to the reviewer of this paper, Dr. Evgeny Smirnov, for comments and suggestions that significantly increased the quality of this work. This work was supported by the 'Preparing for Astrophysics with LSST Program', funded by the Heising-Simons Foundation through grant 2021-2975, and administered by Las Cumbres Observatory. VC would like to thank the Brazilian National Research Council (CNPq, grant 304168/2021-1). GC acknowledges the support from São Paulo Research Foundation (FAPESP, grant 2021/08274-9). This research has made use of the Asteroid Families Portal maintained at the Department of Astronomy/University of Belgrade. This is a publication from the MASB (Machine-learning applied to small bodies, https://valeriocarruba.github.io/Site-MASB/) research group. Questions on this paper can also be sent to the group email address: *mlasb2021@gmail.com*.

DATA AVAILABILITY

Data sets for osculating and filtered images of resonant arguments of asteroids interacting with the $s - s_6 - g_5 + g_6$ (S10) secular resonance are available at the link:

https://drive.google.com/drive/folders/1M5E-ejwS3r49gMA88cWLe3rhjPtCMmF8?usp=sharing

A GitHub repository for the developed codes that produce images of filtered resonant arguments is available at this link:

https://github.com/valeriocarruba/Digital-filtering-for-deep-learning-classification-of-asteroids-in-secular-resonances-

REFERENCES

Brownlee J., 2020, Imbalanced Classification with Python. Ed. Machine Learning Mastery, San Juan, PR, USA
Butterworth S., 1930, Wirel. Eng., 7, 536
Carruba V., 2009, MNRAS, 395, 358
Carruba V., Michtchenko T., 2007, A&A, 475, 1145
Carruba V., Aljbaae S., Domingos R. C., Huaman M., Barletta W., 2021a, Celest. Mech. Dyn. Astron., 133, 38
Carruba V., Aljbaae S., Domingos R. C., 2021b, Celest. Mech. Dyn. Astron., 133, 24
Carruba V., Aljbaae S., Domingos R. C., Barletta W., 2021c, MNRAS, 504, 692
Carruba V., Aljbaae S., Caritá G., Domingos R. C., Martins B., 2022, Celest. Mech. Dyn. Astron., 134, 59
Carruba V., Aljbaae S., Caritá G., Lourenço M. V. F., Martins B. S., Alves A. A., 2023, Front. Astron. Space Sci., 10, 1196223
Carruba V. et al., 2024, MNRAS, 528, 796
Celletti A., Perozzi E., 2020, Celestial Mechanics: The Waltz of the Planets. Springer, New York, NY, USA
Chen P. W., Wang J. Y., Lee H., 2004, 2004 IEEE international joint conference on neural networks (IEEE Cat No04CH37541). New York, NY, USA, p. 2035,
He K., Zhang X., Ren S., Sun J., 2016, 2016 IEEE Conference on Computer Vision and Pattern Recognition (CVPR). Deep Residual Learning for Image Recognition, Las Vegas, NV, USA, p. 770
Jones R. L., Jurić M., Ivezić Z., 2015, Proc. Int. Astron. Union, 10, 282
Knežević Z., 2022, Serbian AJ, 2022, 1
Kolmogorov A. N., 1933, G. dell'Istituto Ital. degli Attuari, 4, 83
Murray C. D., Dermott S. F., 1999, Solar System Dynamics. Cambridge Univ. Press, Cambridge
Novaković B., Vokrouhlický D., Spoto F., Nesvorný D., 2022, Celest. Mech. Dyn. Astron., 134, 34
Pedregosa F. et al., 2011, J. Mach. Learn. Res., 12, 2825
Radović V., Novaković B., Carruba V., Marčeta D., 2017, MNRAS, 470, 576
Simonyan K., Zisserman A., 2014, preprint (arXiv:1409.1556)
Smirnov E. A., 2023, Astron. Comput., 43, 100707
Szegedy C. et al., 2015, Proceedings of the IEEE conference on computer vision and pattern recognition. New York, NY, USA, p. 1
Wolf M., 1898, Astron. Nachr., 148, 383

APPENDIX A: RESULTS OF CNN METHODS

The next tables report results of CNN models for the S2 (Table A1), S4 (Table A2), and S11 (Table A3) resonance data bases.

Table A1. Classification in terms of accuracy, precision, recall, and F1-score for the results obtained by CNN models for samples of unfiltered (U) and filtered (F) images of the S2 resonant arguments. The last three columns report the execution time, memory, maximum memory allocation observed using an 11th Gen Intel(R) Core(TM) i7-11700F @ 2.50GHz CPU. Memory allocations are measured in gigabytes (GB).

Model	Accuracy	Precision	Recall	F1	Time [m:s]	Memory alloc. [GB]	Max. Memory alloc. [GB]
VGG (U)	72.0	71.4	65.2	68.2	5:05	1.54	4.11
VGG+DA (U)	62.0	58.3	60.9	59.6	6:41	1.75	4.32
VGG+DA+DO (U)	58.0	53.6	65.2	58.8	7:12	1.54	4.11
Inception (U)	54.0	–	–	–	5:58	1.75	3.51
Inception+DA (U)	54.0	–	–	–	6:22	1.75	3.51
Inception+DA+DO (U)	54.0	50.0	43.5	46.5	3:54	1.55	3.51
ResNet (U)	64.0	60.0	65.2	62.5	7:55	1.54	8.09
ResNet+DA (U)	46.0	45.8	95.7	62.0	7:30	1.75	8.31
ResNet+DA+DO (U)	62.0	59.1	56.5	57.8	7:53	1.55	8.10
VGG (F)	82.0	81.8	78.3	80.0	5:05	1.54	4.11
VGG+DA (F)	82.0	81.8	78.3	80.0	7:23	1.75	4.31
VGG+DA+DO (F)	82.0	81.8	78.3	80.0	7:06	1.55	4.11
Inception (F)	82.0	81.8	78.3	80.0	5:54	1.54	3.51
Inception+DA (F)	82.0	81.8	78.3	80.0	6:17	1.75	3.51
Inception+DA+DO (F)	82.0	81.8	78.3	80.0	5:43	1.55	3.51
ResNet (F)	82.0	81.8	78.3	80.0	7:38	1.54	8.09
ResNet+DA (F)	82.0	81.8	78.3	80.0	7:15	1.55	8.10
ResNet+DA+DO (F)	82.0	81.8	78.3	80.0	7:46	1.55	8.10

Table A2. Classification in terms of accuracy, precision, recall, and F1-score for the results obtained by CNN models for samples of unfiltered (U) and filtered (F) images of the S4 resonant arguments. The format is the same as Table A1.

Model	Accuracy	Precision	Recall	F1	Time [m:s]	Memory alloc. [GB]	Max. Memory alloc. [GB]
VGG (U)	90.0	0.0	0.0	–	7:10	1.60	4.16
VGG+DA (U)	90.0	0.0	0.0	–	6:08	1.60	4.17
VGG+DA+DO (U)	90.0	0.0	0.0	–	6:49	1.82	4.38
Inception (U)	84.0	14.3	33.3	20.0	8:23	1.60	3.68
Inception+DA (U)	94.0	–	–	–	6:42	1.61	3.68
Inception+DA+DO (U)	94.0	–	–	–	6:30	1.61	3.68
ResNet (U)	94.0	–	0.0	–	6:30	1.60	8.16
ResNet+DA (U)	94.0	–	0.0	–	7:57	1.60	8.16
ResNet+DA+DO (U)	94.0	–	0.0	–	8:48	1.60	8.16
VGG (F)	90.0	37.5	100.0	54.5	7:15	1.60	4.16
VGG+DA (F)	88.0	20.0	33.3	25.0	6:23	2.36	4.92
VGG+DA+DO (F)	84.0	0.0	0.0	–	6:44	1.82	4.39
Inception (F)	86.0	25.0	66.7	36.4	7:44	1.82	3.68
Inception+DA (F)	90.0	33.3	66.7	44.4	6:38	1.82	3.68
Inception+DA+DO (F)	92.0	33.3	33.3	33,3	6:26	1.82	3.68
ResNet (F)	94.0	50.0	100.0	66.7	8:34	1.60	8.16
ResNet+DA (F)	94.0	–	0.0	–	7:56	1.60	8.16
ResNet+DA+DO (F)	94.0	–	0.0	–	8:31	1.60	8.16

Table A3. Classification in terms of accuracy, precision, recall, and F1-score for the results obtained by CNN models for samples of unfiltered (U) and filtered (F) images of the S11 resonant arguments. The format is the same as Table A1.

Model	Accuracy	Precision	Recall	F1	Time [m:s]	Memory alloc. [GB]	Max. Memory alloc. [GB]
VGG (U)	88.0	100.0	14.3	25.0	8:24	2.13	5.29
VGG+DA (U)	86.0	–	0.0	–	6:59	2.34	5.29
VGG+DA+DO (U)	86.0	–	0.0	–	8:56	2.13	5.29
Inception (U)	86.0	50.0	14.3	22.0	10:23	2.49	5.29
Inception+DA (U)	86.0	–	0.0	–	9:23	2.14	5.29
Inception+DA+DO (U)	86.0	–	0.0	–	9:56	2.14	5.29
ResNet (U)	86.0	–	0.0	–	11:18	2.13	8.69
ResNet+DA (U)	86.0	–	0.0	–	11:30	2.14	8.69
ResNet+DA+DO (U)	86.0	–	0.0	–	13:24	2.14	8.69
VGG (F)	96.0	100.0	71.4	83.3	8:34	2.13	5.29
VGG+DA (F)	88.0	100.0	14.3	25.0	7:26	2.14	5.29
VGG+DA+DO (F)	84.0	0.0	0.0	–	9:04	2.34	5.29
Inception (F)	86.0	25.0	66.7	36.4	9:53	2.34	5.29
Inception+DA (F)	92.0	100.0	42.9	60.0	9:35	2.49	5.29
Inception+DA+DO (F)	90.0	100.0	28.6	44.4	9:19	2.34	5.29
ResNet (F)	90.0	100.0	28.6	44.4	11:38	2.13	8.69
ResNet+DA (F)	84.0	0.0	0.0	–	11:24	2.14	8.70
ResNet+DA+DO (F)	76.0	36.8	100.0	53.8	12:53	2.14	8.69

This paper has been typeset from a TEX/LATEX file prepared by the author.